

Cite this: *J. Mater. Chem. A*, 2017, 5, 4513

Template synthesis of CoSe₂/Co₃Se₄ nanotubes: tuning of their crystal structures for photovoltaics and hydrogen evolution in alkaline medium†

Hongmei Li, Xing Qian,* Changli Zhu, Xiancai Jiang, Li Shao and Linxi Hou*

Tubular-structured nanomaterials with tailorable crystal structures and shell architectures whose properties can be tuned without changing their chemical compositions are attractive in electrochemical energy conversion and storage fields. Herein, we report the fabrication of tubular-structured orthorhombic CoSe₂ (o-CoSe₂) and cubic CoSe₂ (c-CoSe₂) by calcining monoclinic Co₃Se₄ nanotubes (Co₃Se₄ NTs) prepared by a facile precursor transformation method. Benefiting from advantageous structural features, including functional shells and well-defined interior voids, the tubular-structured o-CoSe₂ showed a high power conversion efficiency of 9.34% as a counter electrode catalyst for dye-sensitized solar cells (DSSCs), superior to that of a Pt counter electrode (8.15%), under AM 1.5 G irradiation. In addition, the o-CoSe₂ nanotubes also demonstrated excellent electrocatalytic activity in terms of low onset overpotential (~54 mV) and small Tafel slope (~65.9 mV per decade) as a hydrogen evolution reaction (HER) catalyst in alkaline medium. Hence, this work provides a promising strategy to selectively design and synthesize highly active electrocatalysts for energy conversion.

Received 13th December 2016
Accepted 25th January 2017

DOI: 10.1039/c6ta10718d

rsc.li/materials-a

Introduction

In the wake of growing global energy demand and environmental degradation, it is increasingly necessary to develop clean and renewable energy sources based on sustainable electrochemical energy conversion and storage technologies.^{1–4} Among various energy conversion technologies, dye-sensitized solar cells (DSSCs) and water electrolysis have attracted significant attention due to their remarkable merits, such as low cost, high efficiency, and environmentally friendly characteristics, which are highly dependent on the catalytic properties of the electrode materials.^{5–10} Traditionally, Pt-based electrode materials have performed well in catalytic processes for both DSSC and water electrolysis; however, the problems of high cost and low reserves restrict the applications of these materials on a large scale.^{11–14} Therefore, developing highly efficient and promising substitutes based on Earth-abundant elements to replace Pt-based catalysts for both DSSC and the hydrogen evolution reaction (HER) is of great importance and desirability.

In the past few years, driven by their superior magnetic, electrical, optical and catalytic properties, transition metal chalcogenides (TMC) have been regarded as promising precious

metal substitutes for various applications.^{15–19} Among these, cobalt diselenide (CoSe₂) is known for its two main crystal structures, including orthorhombic marcasite-type (denoted as o-CoSe₂) and cubic pyrite-type (denoted as c-CoSe₂); these have been widely investigated in the fields of DSSCs and HER owing to their fascinating characteristics.^{20–24} Usually, o-CoSe₂ is fabricated at low temperature and is further converted to c-CoSe₂ with increasing transition temperature.²⁵ This phase transformation in CoSe₂ give rise to interesting changes to a series of chemical and physical characteristics; therefore, it could be used to tune these characteristics without changing the chemical composition of the material. In view of the outstanding electrocatalytic properties of CoSe₂ when used as the counter electrode (CE) for DSSCs, CoSe₂ is an effective material for catalyzing the reduction of triiodide; thus, it is a potential low cost substitute for Pt CE.^{20,21} Moreover, CoSe₂ also exhibits high efficiency as an HER catalyst in acidic conditions because of its excellent catalytic activity and good chemical stability.^{26–28} For example, the orthorhombic CoSe₂ nanorods synthesized by Dong *et al.* through a hydrothermal method produced a power conversion efficiency (PCE) of 8.38%, which is superior to that of a Pt CE (7.83%).²¹ In addition, Zhang *et al.* reported polymorphic CoSe₂ (p-CoSe₂) with mixed orthorhombic and cubic phases as a highly active electrocatalyst for HER in acidic solution.²⁵ However, despite the fact that great progress in DSSCs and acidic HER has been achieved, no report of the two different phases of CoSe₂ as a bifunctional electrocatalyst has yet demonstrated outstanding catalytic activity comparable to that of Pt-based catalysts for both DSSC and HER

College of Chemical Engineering, Fuzhou University, Xueyuan Road No. 2, Fuzhou 350116, China. E-mail: xingqian@fzu.edu.cn; lxhou@fzu.edu.cn; Fax: +86-0591-2286-6244; Tel: +86-0591-2286-5220

† Electronic supplementary information (ESI) available: XRD pattern, SEM images, TEM images, BET isotherm and comparison list of HER performance. See DOI: 10.1039/c6ta10718d

in alkaline medium. Moreover, the growth mechanisms of the two different phases of CoSe₂ have seldom been discussed in detail.

In addition to the change in crystal structure, the catalytic performance of an electrode material also deeply depends on its unique morphology.²⁹ To date, numerous efforts have been devoted to designing and preparing highly efficient electrocatalysts with diverse, well-defined hollow structures.^{30,31} Due to their advantageous structural features, such as high surface-to-volume ratio, large surface area and low density, these hollow structures have been the subject of extensive research interest for supercapacitors,³² water electrolysis,^{33,34} DSSCs^{35,36} and lithium-ion batteries.³⁷ Particularly, one dimensional (1D) hollow tubular structures, possessing functional shells and well-defined interior voids, are considered to be promising hollow structures. For example, Lou and co-workers reported the design and synthesis of uniform 1D M_xCo_{3-x}S₄ (M = Ni, Mn, Zn) hollow tubular structures using soft polymeric nanofibers as a template; these structures exhibited exceptional electrochemical performance for hybrid supercapacitors.³⁸ However, it is still a sizeable challenge to develop an effective approach for the fabrication of metal selenides with hollow tubular structures, although many efforts have been made. Significantly, tubular structures with massive nanoscale-sized pores can shorten diffusion pathways and improve the total surface area exposed to the electrolyte, thus endowing the structures with high power conversion efficiency for DSSCs.^{39,40} With respect to HER, porous tubular structures embedded with numerous tiny nanostructures can provide large surface areas and rich electroactive sites for electrochemical reactions and thereby enhance the catalytic activity of the structures for HER.⁴¹ Due to these unique structural merits, various tubular-structured functional materials have been widely researched to further improve their performance in different applications; these include Co₉S₈,^{40,42} Mo₂C,⁴¹ CoS_{1.097},⁴³ Co_{0.85}Se⁴⁴ and WS_{2(1-x)-x}Se_{2x}.⁴⁵ To the extent of our knowledge, the fabrication of hollow tubular-structured CoSe₂ and Co₃Se₄ has not been reported by other research groups. Therefore, it is highly desirable to fabricate tubular-structured CoSe₂/Co₃Se₄ and study their applications in DSSCs, especially in alkaline-medium HER.

Herein, we report the synthesis of o-CoSe₂ and c-CoSe₂ tubular structures by calcining monoclinic Co₃Se₄ nanotubes (denoted as Co₃Se₄ NTs) fabricated by a facile precursor transformation method. First, the monoclinic Co₃Se₄ NTs were prepared by hydrothermal treatment of Co(CO₃)_{0.35}-Cl_{0.20}(OH)_{1.10}·1.74H₂O nanorods (denoted as Co precursors) in selenide solution. The as-obtained Co₃Se₄ NTs were then converted to o-CoSe₂ and c-CoSe₂ tubular structures after being calcined at different temperatures in Ar atmosphere. In the synthetic process, it was found that the crystal structure and surface morphology of CoSe₂ can be adjusted by the calcination temperature. As expected, benefiting from their unique structural merits, the o-CoSe₂ nanotubes showed higher catalytic activity for DSSCs and HER in alkaline medium in comparison with c-CoSe₂ NTs, Co₃Se₄ NTs and Co₃Se₄ nanoparticles (denoted as Co₃Se₄ NPs). When used as the counter electrode in DSSCs, the o-CoSe₂ nanotubes exhibited an impressive PCE of

9.34%, superior to that of a Pt CE (8.15%). In addition, the o-CoSe₂ nanotubes also delivered exceptional efficiency as an HER catalyst with an onset overpotential of ~54 mV and a Tafel slope of ~65.9 mV per decade in 1.0 M KOH solution.

Experimental

Materials

Cobalt chloride hexahydrate (CoCl₂·6H₂O, Aladdin Chemistry Co., Ltd, AR), urea (CO(NH₂)₂, Aladdin Chemistry Co., Ltd, AR), hydrazine hydrate (N₂H₄·H₂O, Aladdin Chemistry Co., Ltd, 80%), sodium selenite (Na₂SeO₃, Alfa Aesar, ≥99%), potassium hydroxide (KOH, Aladdin Chemistry Co., Ltd, GR), Nafion solution (Sigma-Aldrich, 5 wt%), Pt/C (Shanghai Hesen Electric Co., Ltd, 20 wt%), absolute ethanol (CH₃CH₂OH, Tianjin Zhiyuan Chemical Reagent Co., Ltd, ≥99.7%), 4-*tert*-butyl pyridine (C₉H₁₃N, Accela ChemBio Co., Ltd, ≥96%), titanium tetrachloride (TiCl₄, Aladdin Chemistry Co., Ltd, AR), lithium perchlorate (LiClO₄, Aladdin Chemistry Co., Ltd, ≥99.9%), iodine (I₂, Shanghai Macklin Biochemical Technology Co., Ltd, ≥99.8%), lithium iodide (LiI, Shanghai Macklin Biochemical Technology Co., Ltd, ≥99%), acetonitrile (CH₃CN, Sinopharm Chemical Reagent Co., Ltd, ≥99%) and 1,2-dimethyl-3-propylimidazolium iodide (DMPPI, Wuhan Lattice Solar Energy Technology Co., Ltd, 99%) were used directly without any further purification. The deionized water used throughout all the experiments was purified using a Millipore system. The N719 dye was obtained from Solarinox Ltd. (Switzerland). The sheet resistance of the FTO glass purchased from Nippon Sheet Glass (Japan) was 15 Ω sq.⁻¹. The used FTO glasses were cut into small plates (1.5 × 1.5 cm²) before ultrasonic cleaning (using cleaner, acetone and alcohol).

Synthesis of Co(CO₃)_{0.35}Cl_{0.20}(OH)_{1.10}·1.74H₂O nanorods

In a typical procedure, 1.2 g of CoCl₂·6H₂O and 0.30 g of urea were firstly dissolved in 60 mL deionized water, and the solution was stirred intensely for 15 min. Then, the above solution was poured into a Teflon-lined stainless steel autoclave with a volume of 100 mL and heated at 140 °C in an air oven for 10 h. After cooling naturally to ambient temperature, the pink precipitates were centrifuged and washed respectively with distilled water and ethanol three times. Finally, after being dried at 60 °C under vacuum for 12 h, 0.56 g of Co(CO₃)_{0.35}-Cl_{0.20}(OH)_{1.10}·1.74H₂O was obtained (yield: 81%).

Synthesis of Co₃Se₄ nanotubes

In a typical procedure, 0.10 g of the Co(CO₃)_{0.35}Cl_{0.20}(OH)_{1.10}·1.74H₂O nanorods and 0.30 g of Na₂SeO₃ were dissolved in 50 mL of deionized water. After that, 10 mL of N₂H₄·H₂O (80%) was added to the solution, and the solution was stirred for 15 min. Then, the above solution was poured into a Teflon-lined stainless steel autoclave with a volume of 100 mL and heated at 180 °C in an air oven for 8 h. After cooling naturally to ambient temperature, the black precipitates were centrifuged and washed respectively with distilled water and ethanol three times. Finally, after being dried at 60 °C under vacuum for 12 h, 0.098 g of Co₃Se₄ NTs was obtained (yield: 82%).

Synthesis of Co₃Se₄ nanoparticles

The Co₃Se₄ nanoparticles were synthesized by a one-step hydrothermal method without adding urea. Typically, 0.10 g of CoCl₂·6H₂O and 0.30 g of Na₂SeO₃ were dispersed in 50 mL of deionized water. After that, 10 mL of N₂H₄·H₂O (80%) was added to the solution, and the solution was stirred for 15 min. Then, the above solution was poured into a Teflon-lined stainless steel autoclave with a volume of 100 mL and heated at 180 °C in an air oven for 10 h. After cooling naturally to ambient temperature, the black precipitates were centrifuged and washed respectively with distilled water and ethanol three times. Finally, after being dried at 60 °C under vacuum for 12 h, 0.058 g of Co₃Se₄ NPs was obtained (yield: 84%).

Synthesis of orthorhombic CoSe₂ nanotubes

Typically, 0.10 g of the as-synthesized Co₃Se₄ NTs was transferred into a porcelain boat and placed in the centre of a tube furnace; the NTs were then heated to 300 °C at a heating rate of 2 °C min⁻¹ and maintained for 2 h in Ar atmosphere. After the furnace was cooled to ambient temperature, 0.088 g of orthorhombic CoSe₂ was collected (yield: 88%).

Synthesis of cubic CoSe₂ nanotubes

Typically, 0.10 g of the as-synthesized Co₃Se₄ NTs was transferred into a porcelain boat and placed in the centre of a tube furnace; the NTs were then heated to 600 °C at a heating rate of 2 °C min⁻¹ and maintained for 2 h in Ar atmosphere. After the furnace was cooled to ambient temperature, 0.083 g of the cubic CoSe₂ sample was collected (yield: 83%).

Electrode preparation

(1) Dye-sensitized solar cells. The counter electrodes were prepared on FTO glass substrates (1.5 × 1.5 cm²) by a spin-casting technique. To directly compare the catalytic activity of the as-obtained samples, the loading amount and thickness of the CE films should be approximately controlled. Briefly, 0.1 g of the as-obtained samples were dispersed in 10 mL of ethyl alcohol (0.01 g mL⁻¹) and sonicated for 30 min to form a homogenous ink suspension. Then, 50 μL of suspension was coated on a FTO glass substrate by spin-casting at 500 rpm for 12 s and subsequently heated at 150 °C for 15 min to remove ethanol. Finally, the resulting CE films were obtained after the second layer was coated using the same processes. The loading mass for each sample was approximately 0.45 mg cm⁻² on a FTO glass substrate. In addition, as a reference, Pt CE was prepared by spin-casting 20 mM chloroplatinic acid (isopropanol solution) on the FTO glass and then annealing at 450 °C for 30 min in air.

(2) Hydrogen evolution reaction. Typically, 2 mg of catalyst and 40 μL of Nafion solution (5 wt%) were dispensed in 460 μL of water/ethanol (v/v = 4 : 1) and then sonicated for 30 min to form a homogenous ink solution. Subsequently, 5 μL of ink catalyst was dropped onto a glass carbon electrode (GCE, 3 mm in diameter) and dried at room temperature. The loading mass

of the catalyst was about 0.283 mg cm⁻². In addition, commercial 20% Pt/C was used as a reference in HER.

Fabrication of DSSCs

TiO₂ photoanodes containing a transparent nanocrystalline layer (~12 μm) and a scattering layer (~4 μm) were prepared by the screen-printing method described in our previous work.^{46,47} The resulting TiO₂ photoanodes were immersed in 0.3 mM N719 dye ethanol solution and sensitized at room temperature for 12 h. Then, the N719 dye-sensitized TiO₂ photoanode and the CE were spaced with a thermoplastic Surlyn film (50 μm) and sealed *via* hot-pressing. The redox electrolyte was an acetonitrile solution consisting of 0.3 M 1,2-dimethyl-3-propylimidazolium iodide (DMPII), 0.1 M LiI, 0.05 M I₂ and 0.5 M 4-*tert*-butylpyridine; the electrolyte was injected into the interspace between the CE and the TiO₂ photoanode. Finally, a DSSC with a geometric active area of 0.16 cm² was obtained.

Characterization and electrochemical methods

The crystal structures of the samples were characterized by X-ray diffraction (XRD, X'Pert PRO, Cu Kα, λ = 0.1542 nm). Raman spectra of the samples were acquired on a Raman spectrometer (Renishaw, inVia Reflex) with a 532 nm excitation laser. The surface morphologies of the samples were measured with a field-emission scanning electron microscope (FESEM, S-4800, Hitachi) and a transmission electron microscope (TEM, TECNAI G2F20, FEI) equipped with an energy dispersive X-ray spectroscope (EDS). The valence states of c-CoSe₂, o-CoSe₂ and Co₃Se₄ were characterized by X-ray photoelectron spectrometer (XPS) analysis (ESCALAB 250, Mg Ka, USA). Thermogravimetric analysis (TG 209 F3, NETZSCH) was performed under a N₂ atmosphere from ambient temperature to 600 °C at a heating rate of 10 °C min⁻¹. The surface area of the samples was examined with a Brunauer–Emmett–Teller (BET) analyzer (Micromeritics, ASAP 2020M, USA).

All electrochemical measurements were performed on a CHI660E electrochemical workstation.

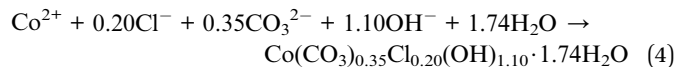
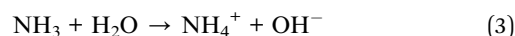
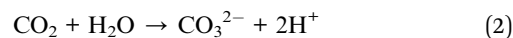
(1) Dye-sensitized solar cells. The photocurrent density–voltage (*J*–*V*) curves of the DSSCs were measured with a standard solar simulator (XM-500W, Trustech) under 100 mW cm⁻² irradiation calibrated with a standard silicon solar cell (91150V, Newport Corporation). Cyclic voltammetry (CV) was performed in a three-electrode electrochemical system (soaked in an anhydrous acetonitrile solution consisting of 10 mM LiI, 1 mM I₂ and 100 mM LiClO₄) and conducted over the scanning potential range from –0.5 V to 0.9 V at different scanning rates. The resulting CE, a Pt sheet and an Ag/AgCl electrode acted as the working electrode, the counter electrode and the reference electrode, respectively. The electrochemical impedance spectra (EIS) and Tafel polarization curves were conducted on symmetrical dummy cells with a sandwich-like structure (CE/electrolyte/CE). The frequency range, bias voltage and AC amplitude of the EIS measurements were 0.1 Hz to 100 kHz, 0 V and 10 mV, respectively. In addition, the Tafel curve tests were performed in the voltage range of –1.0 to 1.0 V at a scan rate of 10 mV s⁻¹. A black mask was applied on the surface of the

DSSCs to avoid stray light, and all solar cell tests were performed at room temperature.

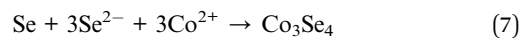
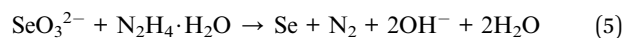
(2) **Hydrogen evolution reaction.** The HER activity was evaluated in a three-electrode electrochemical system using a graphite plate as the counter electrode, an Ag/AgCl electrode as the reference electrode, a glass carbon electrode (GCE, 3 mm in diameter) as the working electrode and 1.0 M KOH aqueous solution as the electrolyte. All the potentials were referenced to a reversible hydrogen electrode (RHE): $E(\text{RHE}) = E(\text{Ag}/\text{AgCl}) + (0.059\text{pH} + 0.205)\text{V}$. Linear sweep voltammetry (LSV), corrected using iR compensation, was conducted in the potential range from -1.8 V to -0.8 V (vs. the Ag/AgCl reference electrode) at a scan rate of 5 mV s^{-1} . The EIS measurements were performed at an overpotential of 150 mV with a frequency range from 0.1 Hz to 100 kHz and an AC amplitude of 5 mV . The long-term stability tests were performed using continuous CV sweeps with a potential range from -0.4 V to -0.1 V vs. RHE at a scan rate of 100 mV s^{-1} . The electrochemical active surface area (ECSA) was determined using cyclic voltammetry in a non-faradaic region from 0.1 to 0.2 V vs. RHE at different scan rates ranging from 10 to 120 mV s^{-1} . The electrochemical double-layer capacitance (C_{dl}) was estimated by plotting $j = j_{\text{anodic}} - j_{\text{cathodic}}$ at 0.15 V vs. RHE against the scan rate. The linear slope is twice the double-layer capacitance (C_{dl}).^{48,49} The amount of hydrogen produced during electrochemical water splitting was measured *via* an online gas chromatograph (GC-2014, Shimadzu).

Results and discussion

The synthetic process of the c-CoSe₂ and o-CoSe₂ nanotubes is shown in Fig. 1. In the first step, CoCl₂·6H₂O was reacted with urea in deionized water at $140\text{ }^\circ\text{C}$ for 10 h to produce Co(CO₃)_{0.35}Cl_{0.20}(OH)_{1.10}·1.74H₂O nanorods. In detail, in the initial stage of the reaction, urea was hydrolyzed in the aqueous solution to yield OH⁻ and CO₃²⁻; also, CoCl₂·6H₂O provided Co²⁺ and Cl⁻. Then, OH⁻, CO₃²⁻ and Cl⁻ reacted with Co²⁺ to form a large number of random nuclei at low temperature. As the reaction temperature and time increased, the high concentration of nuclei was beneficial for accelerating the velocity of nucleation and boosting the growth of crystals. Subsequently, numerous tiny Co(CO₃)_{0.35}Cl_{0.20}(OH)_{1.10}·1.74H₂O crystals aggregated to nanorods. The reaction route in the hydrothermal process can be expressed as follows:⁵⁰



In the next step, the as-prepared Co(CO₃)_{0.35}-Cl_{0.20}(OH)_{1.10}·1.74H₂O nanorods acted as a sacrificial template to fabricate Co₃Se₄ nanotubes through a hydrothermal process in Na₂SeO₃ solution. The formation mechanism of the hollow structures can be explained by the Kirkendall effect.^{51,52} First, water-soluble Na₂SeO₃ was used as the Se source; this can quickly be reduced to Se by hydrazine hydrate, and the newly produced Se is further transformed to Se²⁻. In this system, much elemental Se is still present due to the excess added Na₂SeO₃ and the relatively low pH value in alkaline solution; as a result, not all of the Se was transformed to Se²⁻.⁵³ Subsequently, Se²⁻ ions reacted with the Co²⁺ on the surface of the Co(CO₃)_{0.35}Cl_{0.20}(OH)_{1.10}·1.74H₂O nanorods to form a thin layer of Co₃Se₄. The thin layers, which are composed of plentiful nanocrystallites with many grain boundaries, not only enable the diffusion of materials through the Co₃Se₄ layer but also promote further reaction between Se²⁻ and Co(CO₃)_{0.35}-Cl_{0.20}(OH)_{1.10}·1.74H₂O. According to the Kirkendall effect, where the different diffusivities of atoms in a diffusion couple may give rise to the formation of “Kirkendall voids” close to the interface, the formation of the hollow Co₃Se₄ tubular structures in our case can be ascribed to the fact that the outward diffusion of cobalt ions from the core is faster than the inward diffusion of Se²⁻ from the shell phase through the produced Co₃Se₄ layer.⁴² The corresponding reaction process can be expressed as follows:



Finally, the o-CoSe₂ and c-CoSe₂ samples were synthesized by a chemical transformation method from monoclinic Co₃Se₄ at different calcination temperatures. A possible growth mechanism for o-CoSe₂ and c-CoSe₂ is proposed below. At a lower temperature of $300\text{ }^\circ\text{C}$, the monoclinic Co₃Se₄ was transformed to o-CoSe₂ with well-defined hollow interiors, likely due to the different diffusion rates of cobalt and selenium.³⁷ When the temperature increased to $600\text{ }^\circ\text{C}$, the resulting o-CoSe₂ was further converted to c-CoSe₂ through a phase transformation process. In this process, the tubular-structured o-CoSe₂ was recrystallized, and a small amount of Se element in the c-CoSe₂ sample was gradually evaporated after being heated to a certain temperature; at the same time, the increase of the calcination temperature also resulted in crystal growth and agglomeration of the primary particles in the shells of the nanotubes, realizing

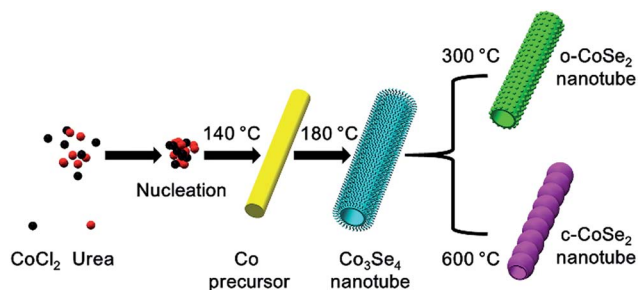


Fig. 1 Schematic of the preparation of the o-CoSe₂ and c-CoSe₂ nanotubes.

the formation of the necklace-like structure of *c*-CoSe₂. In reality, *o*-CoSe₂ and *c*-CoSe₂ possess structural similarity and a small lattice mismatch, leading to facile epitaxial growth between them.^{54,55} In addition, TGA was performed under N₂ atmosphere to understand the decomposition process and relevant phase transitions in cobalt selenide (Fig. S1†). The possible reaction process can be expressed as follows:



The structural information of the as-prepared samples was investigated by XRD and Raman spectroscopy. As shown in Fig. S2 (ESI†), it is clear that all the diffraction peaks in this pattern can be assigned to $\text{Co}(\text{CO}_3)_{0.35}\text{Cl}_{0.20}(\text{OH})_{1.10} \cdot 1.74\text{H}_2\text{O}$ (PDF 00-038-0547). After hydrothermal treatment in selenide solution, all the diffraction peaks of the sample are highly consistent with the monoclinic phase of Co₃Se₄ (PDF 96-901-2805), according to the blue curve in Fig. 2a. For comparison, the XRD pattern of Co₃Se₄ NPs is also presented in Fig. 2a (the olive curve); all the characteristic peaks in this pattern are almost identical to those of the Co₃Se₄ NTs, indicating that they have the same crystal structure. Furthermore, it is worth noting that the intensities of the diffraction peaks of the Co₃Se₄ NTs

are stronger than those of the Co₃Se₄ NPs, which implies the Co₃Se₄ NTs possess better crystallinity. When annealing at 300 °C in Ar atmosphere, the monoclinic Co₃Se₄ nanotubes are converted into pure *o*-CoSe₂, as evidenced from the XRD pattern (the black curve in Fig. 2a), where the main peaks at 30.8, 34.5, 40.0, 47.7, 50.2 and 53.5 can be attributed to the (101), (111), (120), (211), (002) and (031) planes of orthorhombic CoSe₂ (PDF 00-053-0449). When the calcination temperature is increased to 600 °C, prominent reflection peaks are found at 30.5, 34.2, 37.6, 51.7, and 58.9 (the red curve in Fig. 2a), corresponding to the (200), (210), (211), (311), and (321) planes of cubic CoSe₂ (PDF 00-010-0409). The XRD results indicate that the *o*-CoSe₂ and *c*-CoSe₂ samples were successfully prepared *via* chemical transformation of monoclinic Co₃Se₄ NTs at different calcination temperatures.

Fig. 2b shows the Raman spectra of the *o*-CoSe₂, *c*-CoSe₂, and Co₃Se₄ NTs and the Co₃Se₄ NPs. It can be seen that the Raman spectra for all the samples are similar in shape. In detail, the peak at 173 cm⁻¹ can be assigned to the Se–Se stretching mode of *o*-CoSe₂, while the first peaks at 189, 201 and 196 cm⁻¹ of the *c*-CoSe₂ and Co₃Se₄ NTs and the Co₃Se₄ NPs can also be observed, respectively.^{56,57} It is well known that a shift in the first peak can be attributed to a change in the Se–Se bond lengths. In addition, the Raman spectra for *c*-CoSe₂ exhibit three other characteristic peaks located at 468, 510, and 670 cm⁻¹; these are very close to previous reports.⁵⁸ Clearly, the peak position of *o*-CoSe₂ shows a slight shift towards the negative direction in comparison with *c*-CoSe₂. Similarly, the difference in the values of the major peaks of the Co₃Se₄ NTs and the Co₃Se₄ NPs is about 4 cm⁻¹. The phenomenon may be attributed to the quantity effect and the different morphologies of the as-obtained samples.⁵⁹ Furthermore, the similarity of the Raman curves for the five samples is probably due to the fact that all the samples contain cobalt selenide-based phases.

Fig. 3 and S3 (ESI†) show FESEM images of the samples at different magnifications. As shown in Fig. 3a, the panoramic FESEM images show that the $\text{Co}(\text{CO}_3)_{0.35}\text{Cl}_{0.20}(\text{OH})_{1.10} \cdot 1.74\text{H}_2\text{O}$ sample consists of highly uniform nanorods. Clearly, the high-magnification FESEM image (Fig. 3b) exhibits that each nanorod has a smooth surface with an average diameter of about 150 nm. After hydrothermal treatment at 180 °C for 8 h, it can be seen that the Co₃Se₄ sample was successfully synthesized based on the Kirkendall effect and is composed of relatively regular nanotubes with lengths of several micrometers (Fig. 3c). Furthermore, Fig. 3d and e clearly show that these Co₃Se₄ nanotubes have extremely rough surfaces with densely embedded short nanoclusters. Meanwhile, the tubular structures of Co₃Se₄ have diameters of around 300 nm, pore sizes of 200 nm, and wall thicknesses of 50 nm. After the calcination treatment at 300 °C in Ar atmosphere for 2 h, the as-prepared *o*-CoSe₂ samples still show tubular structures; however, numerous aggregated nanoparticles are assembled on the surface (Fig. S3a† and 3f and g), reflecting that the tubular structure possesses good thermal stability. Furthermore, by comparing Fig. 3e and g, it can be found that the pore size of these samples becomes smaller after annealing. When the calcination temperature is increased to 600 °C, it is clearly

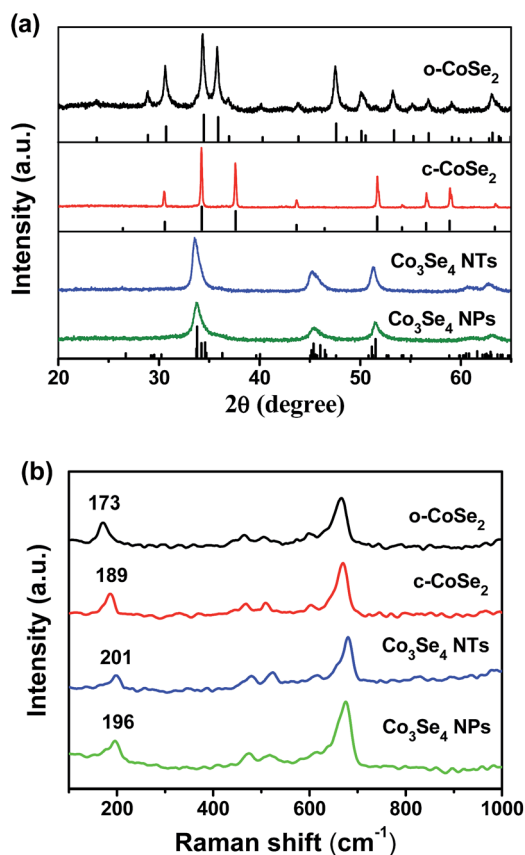


Fig. 2 (a) XRD patterns of the *o*-CoSe₂, *c*-CoSe₂ and Co₃Se₄ NTs and the Co₃Se₄ NPs. (b) Raman spectra of the *o*-CoSe₂, *c*-CoSe₂, and Co₃Se₄ NTs and the Co₃Se₄ NPs.

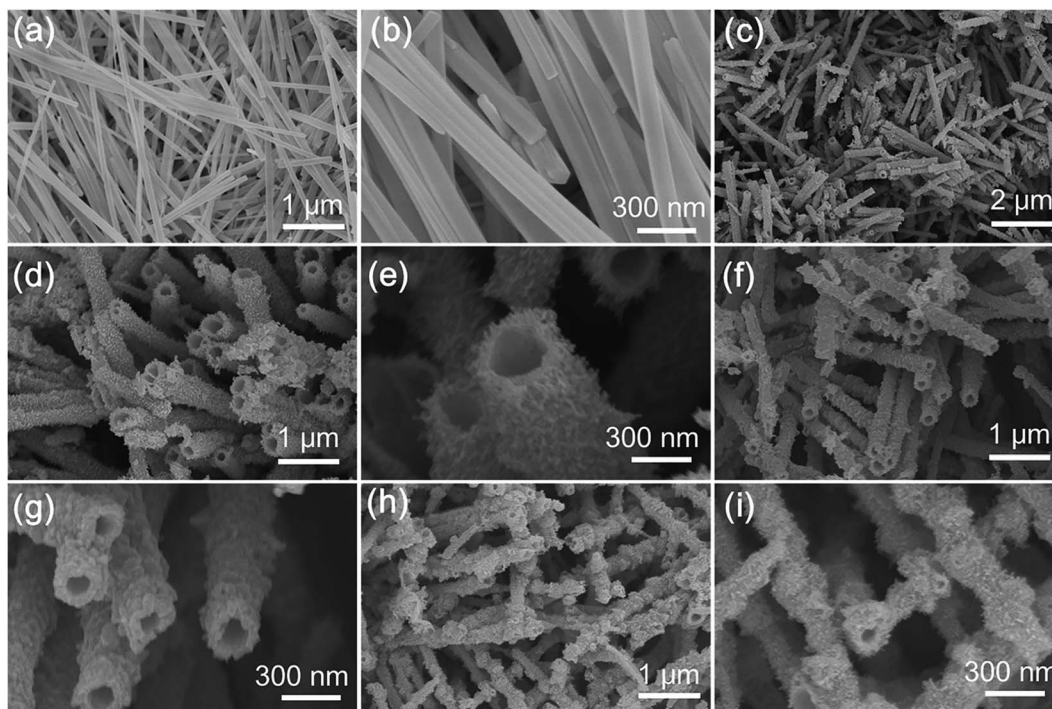


Fig. 3 SEM images of (a and b) $\text{Co}(\text{CO}_3)_{0.35}\text{Cl}_{0.20}(\text{OH})_{1.10}\cdot 1.74\text{H}_2\text{O}$, (c–e) Co_3Se_4 NTs, (f and g) o- CoSe_2 NTs, (h and i) c- CoSe_2 NTs.

observed that the necklace-like c- CoSe_2 inherits the tubular structure and uniformity from Co_3Se_4 and comprises slightly large hollow nanoparticles connected to one another (Fig. 3h and i); this unique necklace-like structure may be related to the fast reaction between the monoclinic Co_3Se_4 nanotubes and selenium vapor at a high calcination temperature.^{22,24} It is noteworthy that the increase of the calcination temperature results in an increase in the particle size of the surfaces of the nanotubes due to the growth and agglomeration of crystal particles.²⁵ In addition, in order to understand the effects of urea on the morphology, $\text{CoCl}_2\cdot 6\text{H}_2\text{O}$ and Na_2SeO_3 were used directly as reactants in the absence of urea to synthesize monoclinic Co_3Se_4 . As can be seen in Fig. S3b,[†] the resulting samples are composed of abundant irregular nanoparticles, implying that urea plays a critical role in the formation of the tubular structures. In this system, these hollow tubular structures constructed of numerous tiny nanostructures can provide more active sites and charge transfer channels, endowing them with higher electrocatalytic activities.

The morphologies and detailed crystal structures of o- CoSe_2 and c- CoSe_2 were further investigated by TEM (Fig. 4 and S4, ESI[†]). The TEM image in Fig. 4a clearly reveals that the as-obtained o- CoSe_2 has a well-defined tubular structure. Furthermore, it can be seen that this well-defined tubular structure is highly porous and has a shell thickness of around 20 to 30 nm (Fig. S4a[†]), which is consistent with the FESEM images of o- CoSe_2 . Fig. 4b exhibits the TEM image of c- CoSe_2 , which has a necklace-like structure constructed of nanoparticles connected to one another. Additionally, it can be clearly seen that the white points are distributed in every nanoparticle, indicating that these nanoparticles with

a diameter of ~ 250 nm are hollow but possess relatively thick shells (Fig. S4b[†]). The high resolution TEM images of o- CoSe_2 and c- CoSe_2 are presented in Fig. 4c and d, respectively. The lattice spacing of 0.290 nm is indexed to the (101) crystal plane of orthorhombic CoSe_2 , while the lattice spacing of 0.336 nm

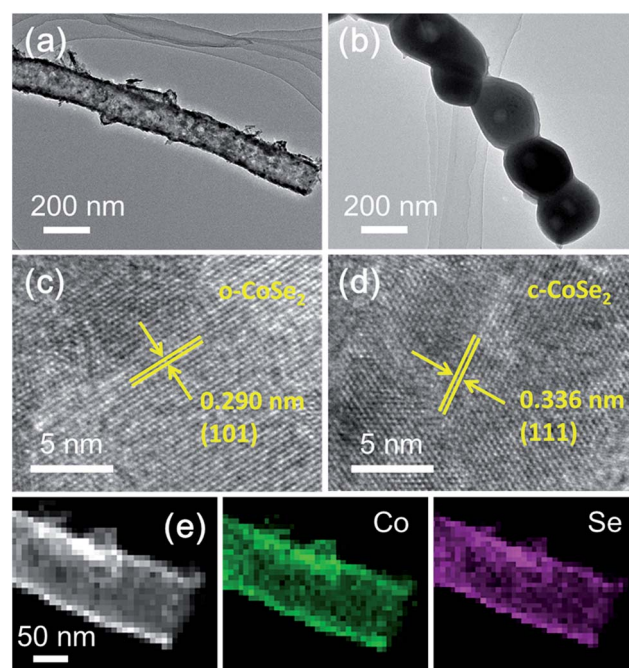


Fig. 4 TEM images of (a and c) o- CoSe_2 , (b and d) c- CoSe_2 . (e) Energy dispersive X-ray (EDX) elemental mapping images of o- CoSe_2 .

corresponds to the (111) crystal plane of cubic CoSe_2 . These results are in good agreement with the above XRD results. As shown in Fig. 4e, the energy dispersive X-ray (EDX) elemental mapping images of *o*- CoSe_2 clearly reflect that the Co and Se elements are uniformly distributed on the shells of the nanotubes.

The valences and chemical compositions of *o*- CoSe_2 , *c*- CoSe_2 , and Co_3Se_4 were investigated and compared through X-ray photoelectron (XPS) measurements. The survey spectra of the three samples are shown in Fig. S5a (ESI[†]), indicating the existence of Co, Se, C (as the reference) and O elements in the surface of this samples; the presence of O elements in all the samples can be ascribed to exposure of the samples to air. Fig. 5a and b reveal the XPS spectra of Co 2p and Se 3d, respectively, for the three samples. It can be found that *o*- CoSe_2 and *c*- CoSe_2 exhibit similar curves in the Co 2p and Se 3d XPS spectra due to their similar elemental valences and chemical compositions. Meanwhile, compared to the XPS spectra of *o*- CoSe_2 and *c*- CoSe_2 , Co_3Se_4 has two spin-orbit doublets in the Co 2p spectrum; also, the binding energy of Se 3d for Co_3Se_4 is slightly shifted to the positive direction, which is attributed to the chemical state change between Co and Se. More precisely, for the *o*- CoSe_2 sample, the Co 2p spectrum in Fig. 5c demonstrates that the dominant peaks at 780.9 eV in Co 2p_{3/2} and 796.7 eV in Co 2p_{1/2} correspond to the Co^{2+} cations in CoSe_2 , of which the peak at 780.9 eV can be ascribed to Co^{2+} cations coordinated with Se ions.^{25,60} As shown in Fig. 5d, the two peaks at 54.5 eV and 55.3 eV can be attributed to Se 3d_{5/2} and Se 3d_{3/2}

of the Co–Se bonds, respectively; the broad peak at 59.1 eV indicates the presence of SeO_x , which is consistent with previous reports.^{55,61} In the case of the Co_3Se_4 NTs, the Co 2p emission spectrum (Fig. 5e) can be fitted into two spin-orbit doublets and two shakeup satellites (marked “sat.”). The peaks at 779.2 eV (Co 2p_{3/2}) and 794.2 eV (Co 2p_{1/2}) are the first doublet corresponding to Co^{3+} , and the peaks observed at 781.1 eV (Co 2p_{3/2}) and 797.3 eV (Co 2p_{1/2}) are the second doublet corresponding to Co^{2+} .^{62,63} presented in Fig. 5f, the binding energies of Se 3d_{5/2} and Se 3d_{3/2} are positively shifted to 54.7 eV and 55.6 eV, respectively, in comparison with that of *o*- CoSe_2 . The broad peak at 59.1 eV is the same as that of *o*- CoSe_2 . This phenomenon shows the obvious chemical state change of Se in the Co_3Se_4 sample. In addition, the high resolution XPS spectra of *c*- CoSe_2 are presented in Fig. S5b and c;† these spectra exhibit similar XPS characteristics to *o*- CoSe_2 because they have the same element valences.

The specific surface area and porosity properties of the as-obtained samples were investigated by nitrogen adsorption-desorption isotherms, and the results are presented in Fig. 6 and S6 (ESI[†]). All the isotherms can be classified as type-IV curves with type-H3 hysteresis loops at a relative pressure of 0.8 to 1.0 p/p_0 , suggesting the existence of mesoporous structures in the samples. The Brunauer–Emmett–Teller (BET) surface areas of the Co_3Se_4 , *o*- CoSe_2 , and *c*- CoSe_2 NTs and the Co_3Se_4 NPs are 32.4, 27.5, 22.1 and 6.2 $\text{m}^2 \text{g}^{-1}$, respectively. Clearly, the Co_3Se_4 NTs have a larger specific surface area than other samples, which may be related to their well-defined tubular structures with shells composed of numerous tiny nanoclusters (as can be seen in the FESEM images of the Co_3Se_4 NTs). In addition, the pore size distributions of the as-obtained samples were calculated by the Barrett–Joyner–Halenda (BJH) method from the two branches of the isotherms. As shown in the inset of Fig. 6, the pore size of *c*- CoSe_2 is 29.9 nm, which is larger than that of *o*- CoSe_2 (28.8 nm) and the Co_3Se_4 NTs (23.0 nm). This result can be ascribed to the crystal growth of the nanostructures in the shell with increasing calcination temperature.⁶⁴ Additionally, the three samples show extremely broad pore size distributions in the range of 5 to 100 nm, indicating that these samples possess massive mesopores and

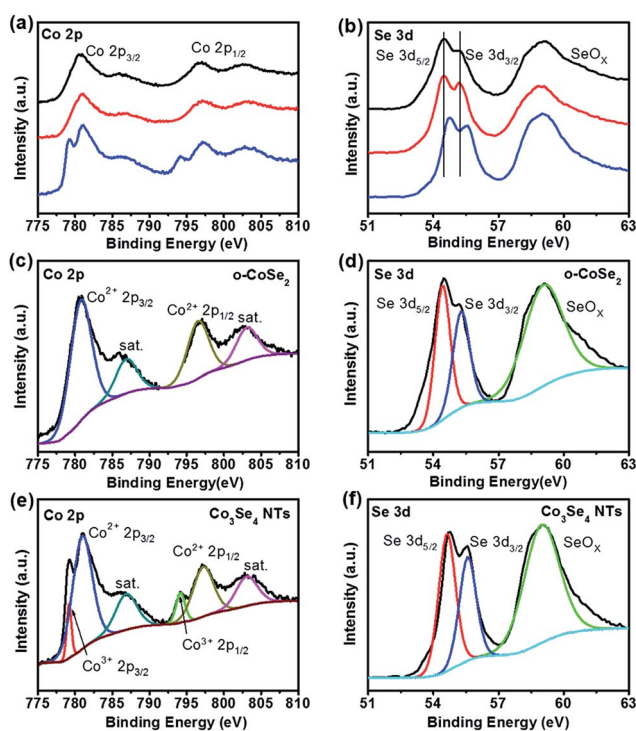


Fig. 5 XPS spectra of (a) Co 2p and (b) Se 3d for *o*- CoSe_2 (black curve), *c*- CoSe_2 (red curve), and the Co_3Se_4 NTs (blue curve). High resolution XPS spectra of (c) Co 2p, (d) Se 3d for *o*- CoSe_2 and (e) Co 2p, (f) Se 3d for the Co_3Se_4 NTs.

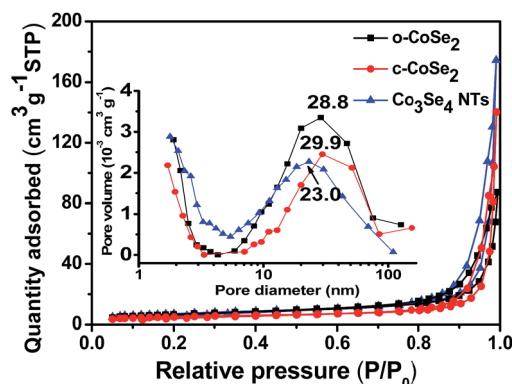


Fig. 6 N_2 adsorption-desorption isotherms and pore size distributions (inset) of the *o*- CoSe_2 , *c*- CoSe_2 , and Co_3Se_4 NTs.

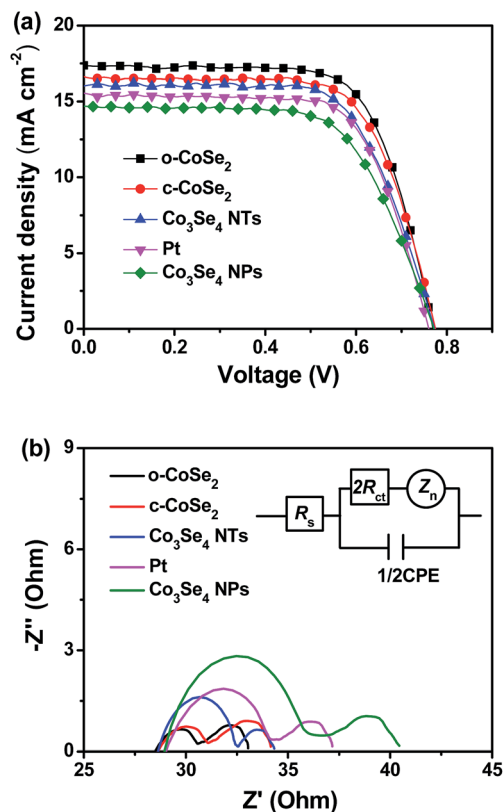


Fig. 7 (a) Photocurrent density–voltage (J – V) curves of the DSSCs with different CEs measured under AM 1.5 G irradiation (100 mW cm^{-2}). (b) Nyquist plots for symmetric cells assembled with different CEs and the corresponding equivalent circuit (inset).

macropores. This tubular structure with a broad pore size distribution can provide a high electroactive surface area and benefit the contact of electroactive materials and electrolyte ions, which is beneficial to enhance the electrocatalytic properties of the materials.⁶⁵

To investigate the photovoltaic properties of DSSCs assembled with the o-CoSe₂, c-CoSe₂, and Co₃Se₄ NTs, Pt, and the Co₃Se₄ NPs, the photocurrent density–voltage (J – V) curves of the cells were measured (Fig. 7a). Meanwhile, the corresponding performance parameters are summarized in Table 1; these include open-circuit voltage (V_{oc}), short-circuit photocurrent density (J_{sc}), fill factor (FF) and power conversion efficiency (PCE). Remarkably, the DSSC based on o-CoSe₂ delivered the highest PCE (9.34%) compared to c-CoSe₂ (8.91%), the Co₃Se₄ NTs (8.44%), Pt (8.15%) and the Co₃Se₄ NPs (7.48%) under the same conditions; the J_{sc} values of the o-CoSe₂, c-CoSe₂ and

Co₃Se₄ NTs, Pt, and the Co₃Se₄ NPs were 17.35, 16.60, 16.10, 15.52 and 14.66 mA cm^{-2} , respectively. The improvement in the PCE can be mainly ascribed to the increase of J_{sc} due to the fast electron transport at the CE/electrolyte interface and the low charge transfer resistance for I_3^- reduction. In detail, the DSSC assembled with the o-CoSe₂ CE yielded a higher PCE and FF (0.70) in comparison with c-CoSe₂ (FF = 0.69), revealing that o-CoSe₂ is a more efficient electrocatalyst with high catalytic activity and charge transfer ability for the reduction of I_3^- ; this may be ascribed to the different structural characteristics of the two phases of CoSe₂. Moreover, the tubular nanostructured o-CoSe₂ surface embedded with more tiny nanoparticles can enhance the surface area that is exposed to the electrolyte. On the other hand, the PCE value of the Co₃Se₄ NTs was higher than that of the Co₃Se₄ NPs because the well-defined tubular structure contributed to higher electrocatalytic activity compared with the amorphous particles, emphasizing the importance of morphology to the electrocatalytic activity.

Electrochemical impedance spectroscopy (EIS) was used to elucidate the electrochemical characteristics of the different CEs; the EIS measurements were conducted on symmetrical dummy cells fabricated with sandwich-like structures (CE/electrolyte/CE). As shown in Fig. 7b, all the Nyquist plots consist of two semicircles in the lower (right) and higher (left) frequency regions, and the equivalent circuit diagrams contain four impedance performance parameters. The high frequency intercepts on the real axis are assigned to the series resistance (R_s), whereas the high frequency semicircle is assigned to the charge transfer resistance (R_{ct}) and the corresponding constant phase element (CPE) at the CE/electrolyte interface. The semicircle in the low frequency range corresponds to the Nernst diffusion limited impedance (Z_n) of the redox couple of in the electrolyte.⁶⁶ The relevant parameters were obtained by fitting the Nyquist plots and are listed in Table 1. Apparently, all the CEs reveal very similar R_s values, which manifests that the effect of the R_s values of the different CEs on their photovoltaic performance can be ignored.¹¹ Therefore, R_{ct} is a very important parameter for assessing the catalytic activity of the counter electrodes. According to Table 1, the sequence of the R_{ct} values is o-CoSe₂ (0.82 Ω) < c-CoSe₂ (0.91 Ω) < Co₃Se₄ NTs (1.62 Ω) < Pt (2.05 Ω) < Co₃Se₄ NPs (3.15 Ω), demonstrating that the catalytic activity decreases in the order of o-CoSe₂ > c-CoSe₂ > Co₃Se₄ NTs > Pt > Co₃Se₄ NPs, which is consistent with the CV data given below. The lowest R_{ct} value was found for the o-CoSe₂ CE, which indicates that it possesses the highest electrocatalytic activity for I_3^- reduction and the fastest electron transfer from the CE to the electrolyte.

Table 1 J – V and EIS parameters of DSSCs with different CEs

CE	V_{oc} (mV)	J_{sc} (mA cm^{-2})	FF	PCE (%)	R_s (ohm)	R_{ct} (ohm)
o-CoSe ₂	771	17.35	0.70	9.34	28.27	0.82
c-CoSe ₂	775	16.60	0.69	8.91	28.38	0.91
Co ₃ Se ₄ NTs	772	16.10	0.68	8.44	28.52	1.62
Pt	762	15.52	0.69	8.15	28.84	2.05
Co ₃ Se ₄ NPs	773	14.66	0.66	7.48	28.86	3.15

The electrocatalytic activities of the different CEs were evaluated by cyclic voltammetry (CV) in a three-electrode system at a scan rate of 50 mV s^{-1} (Fig. 8a). Apparently, all the curves are composed of two typical pairs of oxidation and reduction peaks (Ox-1/Red-1, Ox-2/Red-2). The left and right pairs can be assigned to the oxidation and reduction of I^-/I_3^- (eqn (10)) and I_2/I_3^- (eqn (11)), respectively.^{67,68}



The catalytic ability of the CEs for the reduction of I_3^- to I^- can be evaluated by the left pair of peaks (Ox-1 and Red-1) in the CV curves. Therefore, the peak-to-peak potential separation (E_{pp}) between Red-1 and Ox-1 and the absolute value of peak current intensity ($|J_{\text{Red-1}}|$) are two important parameters for assessing the catalytic activity of a CE (Table 2). The higher $|J_{\text{Red-1}}|$ value reflects the faster catalytic reaction speed, whereas the E_{pp} value is negatively correlated with the standard electrochemical rate constant of a redox reaction. Namely, the higher $|J_{\text{Red-1}}|$ value and lower E_{pp} value indicate better catalytic activity for the reduction of I_3^- .⁶⁹ Compared with the Pt CE, the DSSCs with o-CoSe₂, c-CoSe₂ and Co₃Se₄ NTs CEs exhibited higher $|J_{\text{Red-1}}|$ and lower E_{pp} values, signifying that the electrocatalytic activities of the three electrodes were superior to that of the Pt electrode; this may be due to the fact that the high specific surface areas of the three samples with massive mesopores and macropores are beneficial to the contact and fast diffusion between the CE and

Table 2 CV and Tafel polarization parameters of DSSCs with different CEs

CE	$ J_{\text{Red-1}} $ (mA cm^{-2})	E_{pp} (mV)	$J_{\text{lim}}/$ $\log(\text{mA cm}^{-2})$	$J_0/$ $\log(\text{mA cm}^{-2})$
o-CoSe ₂	1.83	317	1.93	0.69
c-CoSe ₂	1.35	361	1.89	0.58
Co ₃ Se ₄ NTs	1.26	392	1.83	0.49
Pt	1.10	423	1.79	0.43
Co ₃ Se ₄ NPs	0.92	524	1.70	0.34

the electrolyte. In particular, the o-CoSe₂ CE showed the highest $|J_{\text{Red-1}}|$ value and lowest E_{pp} value, suggesting that o-CoSe₂ possesses the best electrocatalytic activity as a CE material for DSSC. Furthermore, considering the lower $|J_{\text{Red-1}}|$ and higher E_{pp} values, the Co₃Se₄ NPs are inferior to Pt and the other Co-based materials and are expected to demonstrate the lowest electrocatalytic activity toward I_3^- reduction. Taking the Co₃Se₄ NTs and o-CoSe₂ as examples, a post-mortem study showed that the tubular morphologies of the Co₃Se₄ NTs and o-CoSe₂ remain almost unaltered after DSSC tests, except that the surface becomes slightly smoother (Fig. S7a and c†).

To elucidate the relationship between the peak current densities (Ox-1 and Red-1) and the scanning rates, the cyclic voltammetry (CV) measurements of the o-CoSe₂ electrode were conducted at different scan rates and are shown in Fig. 8b. As the scanning rates were increased from 10 to 100 mV s^{-1} , the peak current densities increased accordingly; a linear relationship between the peak current density and the square root of

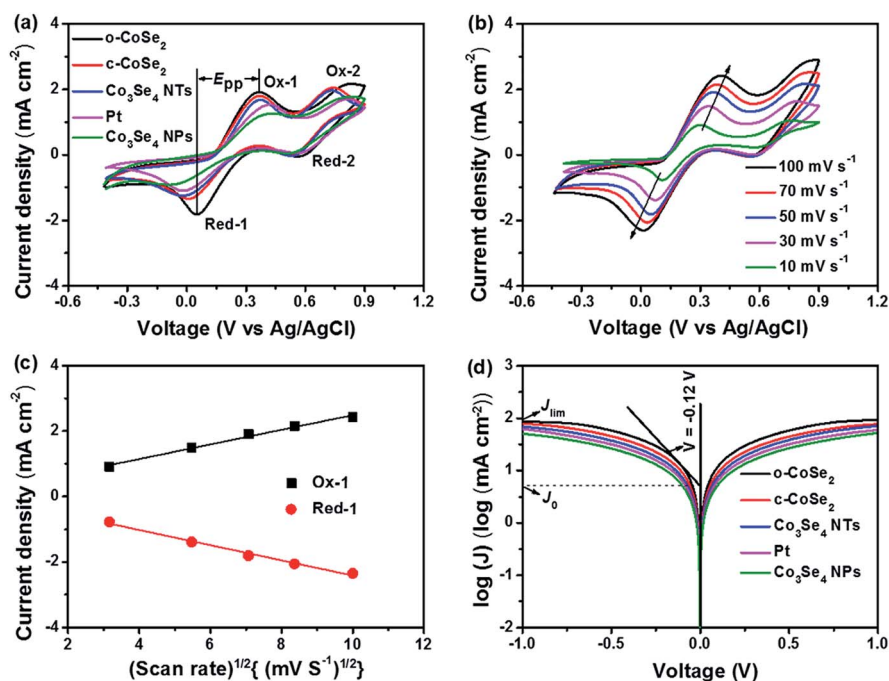


Fig. 8 (a) Cyclic voltammetry (CV) curves of the different CEs at a scan rate of 50 mV s^{-1} . (b) CVs of o-CoSe₂ at different scan rates. (c) The relationship between the redox current densities and the square root of the scan rates. (d) Tafel polarization curves of the symmetric dummy cells with different CEs.

the scanning rate can be observed in Fig. 8c, indicating that the surface of the o-CoSe₂ CE represents the diffusion limitation of the redox reactions and that there is no specific interaction between the I⁻/I₃⁻ redox couple and o-CoSe₂ CE, according to the Langmuir isotherm principle.⁷⁰

The Tafel polarization curves of the different CEs were measured for the symmetric cells used in the EIS experiments. As shown in Fig. 8d, the limiting diffusion current density (J_{lim} , the intersection of the anodic branch with the y axis) and the exchange current density (J_0 , the slope for the anodic or cathodic branch) are closely correlated with the catalytic ability of the CEs (Table 2). A higher J_{lim} reveals a larger ionic diffusion coefficient between the two electrodes based on eqn (12), while a higher J_0 indicates better catalytic activity for I₃⁻ reduction; also, there is a positive correlation between J_0 and R_{ct} based on eqn (13).⁷¹

$$D = lJ_{lim}/2nFC \quad (12)$$

$$J_0 = RT/nFR_{ct} \quad (13)$$

where D is the diffusion coefficient, l is the distance between the two electrodes, F is Faraday's constant, n ($n = 2$) is the number of electrons involved in the reduction of triiodide at the electrode, C is the I₃⁻ concentration, R is the gas constant, T is the temperature (298 K), and R_{ct} is the charge transfer resistance. The J_{lim} decreased in the order of o-CoSe₂ (1.93 log(mA cm⁻²)) > c-CoSe₂ (1.89 log(mA cm⁻²)) > Co₃Se₄ NTs (1.83 log(mA cm⁻²)) > Pt (1.79 log(mA cm⁻²)) > Co₃Se₄ NPs (1.70 log(mA cm⁻²)), indicating that the diffusion coefficients of triiodide for these CEs varied in the positive sequence. On the other hand, the J_0 values also followed the order of o-CoSe₂ > c-CoSe₂ > Co₃Se₄ NTs > Pt > Co₃Se₄ NPs, which is consistent with the R_{ct} trend in the EIS results. This result also demonstrates that the as-obtained o-CoSe₂ electrode has promising potential applications in the field of DSSCs.

A number of Co-based materials have been developed in recent years as non-noble-metal bifunctional electrocatalysts for various applications, especially for alkaline-medium HER and oxygen evolution reaction (OER) processes, owing to their outstanding catalytic activities and exceptional stabilities.^{72–74} Therefore, the as-obtained o-CoSe₂, c-CoSe₂, and Co₃Se₄ NTs and Co₃Se₄ NPs were also tested as electrocatalysts for HER in 1.0 M KOH solution at a scanning rate of 5 mV s⁻¹. Fig. 9a shows the typical polarization curves for all the samples within a cathodic potential, using commercial Pt/C as a reference, which gave an onset overpotential (η_{onset}) of nearly zero at a current density of 1 mA cm⁻². It can be observed that the o-CoSe₂, c-CoSe₂ and Co₃Se₄ NTs exhibited outstanding HER activity in 1.0 M KOH solution based on the overpotentials. Remarkably, o-CoSe₂ delivered a low η_{onset} of 54 mV (*vs.* RHE) at a current density of 1 mA cm⁻², while higher η_{onset} values of 66 and 75 mV were acquired for c-CoSe₂ and the Co₃Se₄ NTs, respectively. Additionally, we tested the HER performance of the Co₃Se₄ NPs; the corresponding η_{onset} was 140 mV at a current density of 1 mA cm⁻², reflecting that this sample demonstrated the lowest HER activity. For HER catalysts, it is necessary to

compare the overpotential demands to drive the current density of 10 mA cm⁻². The corresponding overpotentials (η_{10}) are 124, 149, 184, and 259 mV at a current density of 10 mA cm⁻² for the o-CoSe₂, c-CoSe₂, and Co₃Se₄ NTs and the Co₃Se₄ NPs, respectively. Impressively, the lowest overpotential for o-CoSe₂ indicates that it has superior electrocatalytic properties for HER in alkaline medium; it also outperforms many other non-noble metal-based catalysts, including Ni₂P nanoparticles,⁷⁵ Ni-Co Prussian blue analogue (PBA) nanocubes,⁷⁶ CoP nanowire arrays,⁷⁷ and cobalt nanoparticles encapsulated in nitrogen-carbon.⁷⁸ A detailed comparison is presented in Table S1.†

The inherent properties of the different catalysts were probed by corresponding Tafel plots, in which the linear portion of the Tafel plot is fitted by the Tafel equation ($\eta = b \log j + a$, where b is the Tafel slope and j is the current density).³³ Usually, a small Tafel slope will result in more advantageous electrochemical reaction kinetics. As shown in Fig. 9b, the Tafel slope of commercial Pt/C is 35.2 mV per decade, which is close to the reported value.⁷⁹ Moreover, the Tafel slope for o-CoSe₂ is ~65.9 mV per decade, which is smaller than that of c-CoSe₂ (79.1 mV per decade), Co₃Se₄ NTs (103.7 mV per decade) and Co₃Se₄ NPs (114.7 mV per decade), confirming that o-CoSe₂ possesses favorable reaction kinetics.

To further investigate the kinetics of the as-obtained catalysts at the electrode/electrolyte interface during the HER process, electrochemical impedance spectroscopy (EIS) measurements were performed in 1.0 M KOH solution (Fig. 9c). Clearly, the Nyquist plots for all the electrodes consist of semicircles; the diameter of the semicircle indicates the charge transfer resistance (R_{ct}). A smaller R_{ct} indicates a faster charge transfer capacity.⁷⁶ The R_{ct} value of o-CoSe₂ is 105 Ω , much smaller than the values of 129 Ω , 155 Ω and 269 Ω for o-CoSe₂, Co₃Se₄ NTs and Co₃Se₄ NPs, respectively; this signifies that o-CoSe₂ has favorable kinetics toward H₂ (g) evolution and consequently shows enhanced catalytic activity. In addition, durability is a vital criterion for a good electrocatalyst. Fig. 9d shows a comparison of the polarization curves of o-CoSe₂ before and after CV scanning for 2000 cycles. At the end of cycling, it can be seen that the o-CoSe₂ exhibits similar polarization curves, with a small shift of only around 14 mV at a current density of 10 mA cm⁻²; this indicates that o-CoSe₂ possesses good durability for long-term electrochemical processes. The physical stabilities of the Co₃Se₄ NTs and o-CoSe₂ were further characterized by SEM and XRD (Fig. S7 and S8†). Satisfyingly, the tubular structures of the Co₃Se₄ NTs and o-CoSe₂ were retained. In addition, it can be seen that the surfaces of the Co₃Se₄ NTs and o-CoSe₂ after the HER stability tests were rougher, which may be associated with the stripping of H₂ during the tests. Fig. S8† shows the XRD patterns of Co₃Se₄ NTs and o-CoSe₂ after the HER stability tests. The peak positions can be indexed to Co₃Se₄ NTs (PDF 96-901-2805) and o-CoSe₂ (PDF 00-053-0449). Therefore, the morphologies and compositions of the catalysts were well preserved after the stability tests.

To further investigate the electrochemically active surface area (ECSA) of the electrode, the electrochemical double-layer capacitance (C_{dl}) was estimated by measuring cyclic voltammograms in a non-faradaic region from 0.1 to 0.2 V *vs.* RHE

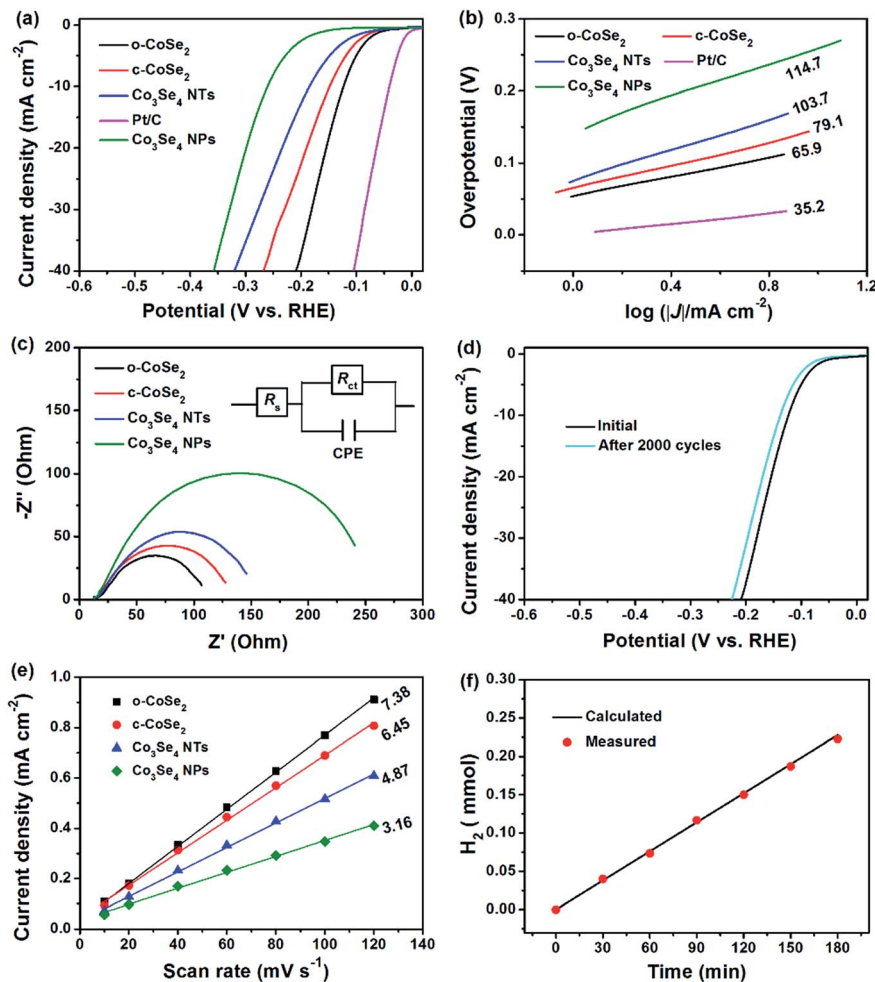


Fig. 9 (a) Polarization curves of the o-CoSe₂, c-CoSe₂, and Co₃Se₄ NTs, Pt/C and the Co₃Se₄ NPs at a scan rate of 5 mV s⁻¹ in 1.0 M KOH solution (b) Tafel plots of the o-CoSe₂, c-CoSe₂, and Co₃Se₄ NTs, Pt/C and the Co₃Se₄ NPs. (c) Nyquist plots of the o-CoSe₂, c-CoSe₂, and Co₃Se₄ NTs and the Co₃Se₄ NPs at an overpotential of 150 mV and the corresponding equivalent circuit (inset). (d) Polarization curves of the o-CoSe₂ NTs before and after 2000 CV cycles with a potential range from -0.4 V to -0.1 V vs. RHE. (e) The C_{dl} of the different samples obtained at 0.15 V vs. RHE. (f) Calculated (solid line) and measured (red dot) amounts of hydrogen at different times for o-CoSe₂ at an overpotential of 250 mV in 1.0 M KOH.⁸⁵

(Fig. S9†).^{80,81} Typically, the C_{dl} is linearly proportional to the ECSA, which can be derived from the slope of the linear relationship between current density and scan rate (Fig. 9e).^{82,83} Apparently, the C_{dl} of o-CoSe₂ (7.38 mF cm⁻²) is larger than that of c-CoSe₂ (6.45 mF cm⁻²), the Co₃Se₄ NTs (4.87 mF cm⁻²) and the Co₃Se₄ NPs (3.16 mF cm⁻²), indicating that o-CoSe₂ possesses more active sites at the solid-liquid interface, which is beneficial for the electrocatalytic performance. Meanwhile, the exchange current densities (J₀) of the different samples were also obtained by the extrapolation of Tafel plots (Fig. S10†) and listed in Table 3, which reflects the intrinsic rate of electron transfer under reversible conditions.⁸⁴ The o-CoSe₂ sample shows an exchange current density of 0.15 mA cm⁻², outperforming the values of 0.13 mA cm⁻², 0.11 mA cm⁻² and 0.08 mA cm⁻² for c-CoSe₂, Co₃Se₄ NTs and Co₃Se₄ NPs, respectively.

We further confirmed the hydrogen generation by gas chromatography (GC) to quantitatively measure the generated hydrogen. Cathodic electrolysis was performed by maintaining

an o-CoSe₂-loaded glassy carbon plate at a static overpotential of 250 mV (vs. RHE) for 180 min. The faradaic efficiency (FE) of the HER process can be obtained by dividing the measured amount of hydrogen with theoretically calculated hydrogen (assuming 100% FE). The agreement of the calculated and measured values (Fig. 9f) indicates that o-CoSe₂ has a FE of nearly 100%.^{85,86}

The above results display the superior electrocatalytic activity of the o-CoSe₂ nanotubes for the DSSC and HER. This superior performance can be chiefly ascribed to the advantageous structural features of the o-CoSe₂ nanotubes. Particularly, the hollow tubular space can be regarded as a reservoir for electrolytes, which is conducive to increase the interior reaction space for fast diffusion and reaction between the electroactive materials and the electrolyte.⁸⁷ Meanwhile, the well-defined tubular structure, with a shell composed of numerous tiny nanoparticles, gives rise to a relatively large surface area and offers abundant electroactive sites for electrochemical

Table 3 The HER performances of the as-obtained catalysts in alkaline medium

Catalyst	η_{onset} (mV)	η_{10} (mV)	b (mV per decade)	R_{ct} (ohm)	C_{dl} (mF cm ⁻²)	J_0 (mA cm ⁻²)
o-CoSe ₂	54	124	65.9	105	7.38	0.15
c-CoSe ₂	66	149	79.1	129	6.45	0.13
Co ₃ Se ₄ NTs	75	184	103.7	155	4.87	0.11
Co ₃ Se ₄ NPs	140	259	114.7	269	3.16	0.08

reactions, resulting in high electrochemical activity.^{41,88} In addition, the open spaces between the nanoparticles and the massive mesopores and macropores existing in the shell can shorten the diffusion paths for both mass and charge transport, thus accelerating the charge transfer at the electrode/electrolyte interface.¹⁹

Conclusions

In summary, we report an effective and promising approach for the synthesis of o-CoSe₂ and c-CoSe₂ tubular structures from Co₃Se₄ nanotubes. The process involves a facile precursor transformation method and a subsequent annealing strategy in Ar atmosphere. As a reference, we also prepared amorphous Co₃Se₄ NPs without adding urea; our results show that urea has an important effect on the morphologies of the samples and ultimately reinforces their electrocatalytic activities. The as-obtained samples were then used as bifunctional electrocatalysts for both DSSCs and HER in alkaline medium, with high catalytic activity. Benefiting from advantageous structural features, the tubular-structured o-CoSe₂ showed particularly excellent electrocatalytic activity for DSSC, producing a PCE of 9.34%; this value is much higher than that of a Pt CE (8.15%). In addition, the tubular-structured o-CoSe₂ also demonstrated a low onset overpotential (~54 mV) and a small Tafel slope (~65.9 mV per decade) as a HER catalyst in alkaline medium. As a demonstration, we expect that this effective and promising approach can be extended to fabricate other advanced electrocatalysts for electrochemical energy conversion technologies by tuning their crystal structures and surface morphologies.

Acknowledgements

This work was financially supported by the National Natural Science Foundation of China (No. 21676057) and the Project of Education Department of Fujian Province (No. JAT160052).

References

- M. R. Gao, Y. F. Xu, J. Jiang and S. H. Yu, *Chem. Soc. Rev.*, 2013, **42**, 2986–3017.
- S. Chu and A. Majumdar, *Nature*, 2012, **488**, 294–303.
- Y. Jiao, Y. Zheng, M. T. Jaroniec and S. Z. Qiao, *Chem. Soc. Rev.*, 2015, **44**, 2060–2086.
- A. S. Arico, P. Bruce, B. Scrosati, J. M. Tarascon and W. Van Schalkwijk, *Nat. Mater.*, 2005, **4**, 366–377.
- A. Hagfeldt, G. Boschloo, L. C. Sun, L. Kloo and H. Pettersson, *Chem. Rev.*, 2010, **110**, 6595–6663.
- Y. Hou, D. Wang, X. H. Yang, W. Q. Fang, B. Zhang, H. F. Wang, G. Z. Lu, P. Hu, H. J. Zhao and H. G. Yang, *Nat. Commun.*, 2013, **4**, 67–88.
- S. Thomas, T. G. Deepak, G. S. Anjusree, T. A. Arun, S. V. Nair and A. S. Nair, *J. Mater. Chem. A*, 2014, **2**, 4474–4490.
- M. S. Faber and S. Jin, *Energy Environ. Sci.*, 2014, **7**, 3519–3542.
- X. X. Zou and Y. Zhang, *Chem. Soc. Rev.*, 2015, **44**, 5148–5180.
- Y. Zheng, Y. Jiao, Y. H. Zhu, L. H. Li, Y. Han, Y. Chen, A. J. Du, M. Jaroniec and S. Z. Qiao, *Nat. Commun.*, 2014, **5**, 4783.
- F. Gong, H. Wang, X. Xu, G. Zhou and Z. S. Wang, *J. Am. Chem. Soc.*, 2012, **134**, 10953–10958.
- M. R. Gao, J. X. Liang, Y. R. Zheng, Y. F. Xu, J. Jiang, Q. Gao, J. Li and S. H. Yu, *Nat. Commun.*, 2015, **6**, 5982–5988.
- S. N. Yun, A. Hagfeldt and T. L. Ma, *Adv. Mater.*, 2014, **26**, 6210–6237.
- X. M. Li, X. G. Hao, A. Abudula and G. Q. Guan, *J. Mater. Chem. A*, 2016, **4**, 11973–12000.
- X. H. Rui, H. T. Tan and Q. Y. Yan, *Nanoscale*, 2014, **6**, 9889–9924.
- M. S. Faber, R. Dziedzic, M. A. Lukowski, N. S. Kaiser, Q. Ding and S. Jin, *J. Am. Chem. Soc.*, 2014, **136**, 10053–10061.
- F. Gong, X. Xu, Z. Li, G. Zhou and Z. S. Wang, *Chem. Commun.*, 2013, **49**, 1437–1439.
- M.-R. Gao, Z.-Y. Lin, T.-T. Zhuang, J. Jiang, Y.-F. Xu, Y.-R. Zheng and S.-H. Yu, *J. Mater. Chem.*, 2012, **22**, 13662–13668.
- S. J. Peng, L. L. Li, H. T. Tan, R. Cai, W. H. Shi, C. C. Li, S. G. Mhaisalkar, M. Srinivasan, S. Ramakrishna and Q. Y. Yan, *Adv. Funct. Mater.*, 2014, **24**, 2155–2162.
- H. Sun, L. Zhang and Z.-S. Wang, *J. Mater. Chem. A*, 2014, **2**, 16023–16029.
- J. Dong, J. H. Wu, J. B. Jia, S. Y. Wu, P. Zhou, Y. G. Tu and Z. Lan, *Electrochim. Acta*, 2015, **168**, 69–75.
- K. Wang, D. Xi, C. J. Zhou, Z. Q. Shi, H. Y. Xia, G. W. Liu and G. J. Qiao, *J. Mater. Chem. A*, 2015, **3**, 9415–9420.
- H. X. Zhang, L. C. Lei and X. W. Zhang, *RSC Adv.*, 2014, **4**, 54344–54348.
- C.-P. Lee, W.-F. Chen, T. Billo, Y.-G. Lin, F.-Y. Fu, S. Samireddi, C.-H. Lee, J.-S. Hwang, K.-H. Chen and L.-C. Chen, *J. Mater. Chem. A*, 2016, **4**, 4553–4561.
- H. X. Zhang, B. Yang, X. L. Wu, Z. J. Li, L. C. Lei and X. W. Zhang, *ACS Appl. Mater. Interfaces*, 2015, **7**, 1772–1779.

- 26 J. H. Wang, W. Cui, Q. Liu, Z. C. Xing, A. M. Asiri and X. P. Sun, *Adv. Mater.*, 2016, **28**, 215–230.
- 27 Y.-R. Zheng, M.-R. Gao, Z.-Y. Yu, Q. Gao, H.-L. Gao and S.-H. Yu, *Chem. Sci.*, 2015, **6**, 4594–4598.
- 28 Q. Liu, J. L. Shi, J. M. Hu, A. M. Asiri, Y. L. Luo and X. P. Sun, *ACS Appl. Mater. Interfaces*, 2015, **7**, 3877–3881.
- 29 C. Burda, X. B. Chen, R. Narayanan and M. A. El-Sayed, *Chem. Rev.*, 2005, **105**, 1025–1102.
- 30 X. W. Lou, L. A. Archer and Z. C. Yang, *Adv. Mater.*, 2008, **20**, 3987–4019.
- 31 Z. K. Chen, D. D. He, X. J. Xu, Z. Z. Liu, M. H. Huang, X. Wang and H. Q. Jiang, *RSC Adv.*, 2016, **6**, 34159–34164.
- 32 C.-Y. Cao, W. Guo, Z.-M. Cui, W.-G. Song and W. Cai, *J. Mater. Chem.*, 2011, **21**, 3204–3209.
- 33 L. Yu, B. Y. Xia, X. Wang and X. W. Lou, *Adv. Mater.*, 2016, **28**, 92.
- 34 Z.-F. Huang, J. J. Song, K. Li, M. Tahir, Y.-T. Wang, L. Pan, L. Wang, X. W. Zhang and J.-J. Zou, *J. Am. Chem. Soc.*, 2016, **138**, 1359–1365.
- 35 Z. H. Dong, X. Y. Lai, J. E. Halpert, N. L. Yang, L. X. Yi, J. Zhai, D. Wang, Z. Y. Tang and L. Jiang, *Adv. Mater.*, 2012, **24**, 1046–1049.
- 36 C.-T. Lee, J.-D. Peng, C.-T. Li, Y.-L. Tsai, R. Vittal and K.-C. Ho, *Nano Energy*, 2014, **10**, 201–211.
- 37 H. Hu, J. T. Zhang, B. Y. Guan and X. W. Lou, *Angew. Chem., Int. Ed.*, 2016, **55**, 9514–9518.
- 38 Y. M. Chen, Z. Li and X. W. Lou, *Angew. Chem., Int. Ed.*, 2015, **54**, 10521–10524.
- 39 M. Jafarzadeh, C. S. Sipaut, J. Dayou and R. F. Mansa, *Renewable Sustainable Energy Rev.*, 2016, **64**, 543–568.
- 40 H.-W. Chen, C.-W. Kung, C.-M. Tseng, T.-C. Wei, N. Sakai, S. Morita, M. Ikegami, T. Miyasaka and K.-C. Ho, *J. Mater. Chem. A*, 2013, **1**, 13759–13768.
- 41 F.-X. Ma, H. B. Wu, B. Y. Xia, C.-Y. Xu and X. W. Lou, *Angew. Chem., Int. Ed.*, 2015, **54**, 15395–15399.
- 42 Z. H. Wang, L. Pan, H. B. Hu and S. P. Zhao, *CrystEngComm*, 2010, **12**, 1899–1904.
- 43 S. G. Liu, C. P. Mao, Y. B. Niu, F. L. Yi, J. K. Hou, S. Y. Lu, J. Jiang, M. W. Xu and C. M. Li, *ACS Appl. Mater. Interfaces*, 2015, **7**, 25568–25573.
- 44 Z. H. Wang, Q. Sha, F. W. Zhang, J. Pu and W. Zhang, *CrystEngComm*, 2013, **15**, 5928–5934.
- 45 K. Xu, F. M. Wang, Z. X. Wang, X. Y. Zhan, Q. S. Wang, Z. Z. Cheng, M. Safdar and J. He, *ACS Nano*, 2014, **8**, 8468–8476.
- 46 X. Qian, H. M. Li, L. Shao, X. C. Jiang and L. X. Hou, *ACS Appl. Mater. Interfaces*, 2016, **8**, 29486–29495.
- 47 X. Qian, L. Shao, H. M. Li, R. C. Yan, X. Y. Wang and L. X. Hou, *J. Power Sources*, 2016, **319**, 39–47.
- 48 B. You and Y. J. Sun, *Adv. Energy Mater.*, 2016, **6**, 1502333.
- 49 B. You, N. Jiang, M. L. Sheng, M. W. Bhushan and Y. J. Sun, *ACS Catal.*, 2016, **6**, 714–721.
- 50 W. X. Guo, C. Chen, M. D. Ye, M. Q. Lv and C. J. Lin, *Nanoscale*, 2014, **6**, 3656–3663.
- 51 H. J. Fan, U. Goesele and M. Zacharias, *Small*, 2007, **3**, 1660–1671.
- 52 B. D. Anderson and J. B. Tracy, *Nanoscale*, 2014, **6**, 12195–12216.
- 53 Z. Zhuang, Q. Peng, J. Zhuang, X. Wang and Y. Li, *Chem.–Eur. J.*, 2005, **12**, 211–217.
- 54 R. Sun, M. K. Y. Chan and G. Ceder, *Phys. Rev. B: Condens. Matter Mater. Phys.*, 2011, **83**, 235311–235322.
- 55 D. S. Kong, H. T. Wang, Z. Y. Lu and Y. Cui, *J. Am. Chem. Soc.*, 2014, **136**, 4897–4900.
- 56 M. Basu, Z.-W. Zhang, C.-J. Chen, P.-T. Chen, K.-C. Yang, C.-G. Ma, C. C. Lin, S.-F. Hu and R.-S. Liu, *Angew. Chem., Int. Ed.*, 2015, **54**, 6211–6216.
- 57 Y. W. Liu, H. Cheng, M. J. Lyu, S. J. Fan, Q. H. Liu, W. S. Zhang, Y. D. Zhi, C. M. Wang, C. Xiao, S. Q. Wei, B. J. Ye and Y. Xie, *J. Am. Chem. Soc.*, 2014, **136**, 15670–15675.
- 58 C. E. M. Campos, J. C. de Lima, T. A. Grandi, K. D. Machado and P. S. Pizani, *Phys. B*, 2002, **324**, 409–418.
- 59 W. D. Shi, X. Zhang and G. B. Che, *Int. J. Hydrogen Energy*, 2013, **38**, 7037–7045.
- 60 L. Liang, H. Cheng, F. C. Lei, J. Han, S. Gao, C. M. Wang, Y. F. Sun, S. Qamar, S. Q. Wei and Y. Xie, *Angew. Chem., Int. Ed.*, 2015, **54**, 12004–12008.
- 61 H. Y. Li, D. Gao and X. Cheng, *Electrochim. Acta*, 2014, **138**, 232–239.
- 62 H. C. Chen, J. J. Jiang, L. Zhang, H. Z. Wan, T. Qi and D. D. Xia, *Nanoscale*, 2013, **5**, 8879–8883.
- 63 J. H. Huo, J. H. Wu, M. Zheng, Y. G. Tu and Z. Lan, *J. Power Sources*, 2016, **304**, 266–272.
- 64 Y. L. Zhou, D. Yan, H. Y. Xu, J. K. Feng, X. L. Jiang, J. Yue, J. Yang and Y. T. Qian, *Nano Energy*, 2015, **12**, 528–537.
- 65 H. C. Chen, J. J. Jiang, Y. D. Zhao, L. Zhang, D. Q. Guo and D. D. Xia, *J. Mater. Chem. A*, 2015, **3**, 428–437.
- 66 Y. H. Wu, B. Zhou, C. Yang, S. C. Liao, W.-H. Zhang and C. Li, *Chem. Commun.*, 2016, **52**, 11488–11491.
- 67 Y.-C. Wang, D.-Y. Wang, Y.-T. Jiang, H.-A. Chen, C.-C. Chen, K.-C. Ho, H.-L. Chou and C.-W. Chen, *Angew. Chem., Int. Ed.*, 2013, **52**, 6694–6698.
- 68 Y. Y. Duan, Q. W. Tang, B. L. He, R. Li and L. M. Yu, *Nanoscale*, 2014, **6**, 12601–12608.
- 69 M. X. Wu, X. Lin, Y. D. Wang, L. Wang, W. Guo, D. D. Qu, X. J. Peng, A. Hagfeldt, M. Graetzel and T. L. Ma, *J. Am. Chem. Soc.*, 2012, **134**, 3419–3428.
- 70 W. J. Wang, X. Pan, W. Q. Liu, B. Zhang, H. W. Chen, X. Q. Fang, J. X. Yao and S. Y. Dai, *Chem. Commun.*, 2014, **50**, 2618–2620.
- 71 Y. Y. Duan, Q. W. Tang, J. Liu, B. L. He and L. M. Yu, *Angew. Chem., Int. Ed.*, 2014, **53**, 14569–14574.
- 72 T. T. Liu, Q. Liu, A. M. Asiri, Y. L. Luo and X. P. Sun, *Chem. Commun.*, 2015, **51**, 16683–16686.
- 73 X. J. Xu, P. Y. Du, Z. K. Chen and M. H. Huang, *J. Mater. Chem. A*, 2016, **4**, 10933–10939.
- 74 D. S. Kong, J. J. Cha, H. T. Wang, H. R. Lee and Y. Cui, *Energy Environ. Sci.*, 2013, **6**, 3553–3558.
- 75 L. G. Feng, H. Vrubel, M. Bensimon and X. Hu, *Phys. Chem. Chem. Phys.*, 2014, **16**, 5917–5921.
- 76 Y. Feng, X.-Y. Yu and U. Paik, *Chem. Commun.*, 2016, **52**, 1633–1636.

- 77 J. Q. Tian, Q. Liu, A. M. Asiri and X. P. Sun, *J. Am. Chem. Soc.*, 2014, **136**, 7587–7590.
- 78 J. Wang, D. F. Gao, G. X. Wang, S. Miao, H. H. Wu, J. Y. Li and X. H. Bao, *J. Mater. Chem. A*, 2014, **2**, 20067–20074.
- 79 L. Shao, X. Qian, X. Y. Wang, H. M. Li, R. C. Yan and L. X. Hou, *Electrochim. Acta*, 2016, **213**, 236–243.
- 80 C. C. L. McCrory, S. Jung, I. M. Ferrer, S. M. Chatman, J. C. Peters and T. F. Jaramillo, *J. Am. Chem. Soc.*, 2015, **137**, 4347–4357.
- 81 N. Jiang, Q. Tang, M. L. Sheng, B. You, D.-E. Jiang and Y. J. Sun, *Catal. Sci. Technol.*, 2016, **6**, 1077–1084.
- 82 B. You, N. Jiang, M. L. Sheng, S. Gul, J. Yano and Y. J. Sun, *Chem. Mater.*, 2015, **27**, 7636–7642.
- 83 B. You, N. Jiang, M. L. Sheng and Y. J. Sun, *Chem. Commun.*, 2015, **51**, 4252–4255.
- 84 Q. Liu, J. Q. Tian, W. Cui, P. Jiang, N. Y. Cheng, A. M. Asiri and X. P. Sun, *Angew. Chem., Int. Ed.*, 2014, **53**, 6710–6714.
- 85 W. Y. Yuan, X. Y. Wang, X. L. Zhong and C. M. Li, *ACS Appl. Mater. Interfaces*, 2016, **8**, 20720–20729.
- 86 B. You, N. Jiang, X. Liu and Y. J. Sun, *Angew. Chem., Int. Ed.*, 2016, **55**, 9913–9917.
- 87 X. Zhang, M. M. Zhen, J. W. Bai, S. W. Jin and L. Lie, *ACS Appl. Mater. Interfaces*, 2016, **8**, 17187–17193.
- 88 L. Yu, B. Y. Guan, W. Xiao and X. W. Lou, *Adv. Energy Mater.*, 2015, **5**, 1500981.